

Mid-infrared supercontinuum and optical frequency comb generations in a multimode tellurite photonic crystal fiber

Xu Han(韩旭), Ying Han(韩颖), Chao Mei(梅超), Jing-Zhao Guan(管景昭), Yan Wang(王彦), Lin Gong(龚琳), Jin-Hui Yuan(苑金辉), and Chong-Xiu Yu(余重秀)

Citation: Chin. Phys. B, 2021, 30 (**9**): 094207. DOI: 10.1088/1674-1056/abf10f
Journal homepage: http://cpb.iphy.ac.cn; http://iopscience.iop.org/cpb

What follows is a list of articles you may be interested in

Design and fabrication of GeAsSeS chalcogenide waveguides with thermal annealing

Limeng Zhang(张李萌), Jinbo Chen(陈锦波), Jierong Gu(顾杰荣), Yixiao Gao(高一骁), Xiang Shen(沈祥), Yimin Chen(陈益敏), and Tiefeng Xu(徐铁峰)

Chin. Phys. B, 2021, 30 (**3**): 034210. DOI: 10.1088/1674-1056/abd757

Role of quantum paths in generation of attosecond pulses

M R Sami and A Shahbaz†

Chin. Phys. B, 2020, 29 (**10**): 104207. DOI: 10.1088/1674-1056/ab9deb

Orientation-dependent depolarization of supercontinuum in BaF_2 crystal

Zi-Xi Li(李子熙), Cheng Gong(龚成), Tian-Jiao Shao(邵天骄), Lin-Qiang Hua(华林强), Xue-Bin Bian(卞学滨), Xiao-Jun Liu(柳晓军)

Chin. Phys. B, 2020, 29 (**1**): 014212. DOI: 10.1088/1674-1056/ab5fc7

The 2-μm to 6-μm mid-infrared supercontinuum generation in cascaded ZBLAN and As_2Se_3 step-index fibers

Jinmei Yao(姚金妹), Bin Zhang(张斌), Ke Yin(殷科), Jing Hou(侯静)

Chin. Phys. B, 2019, 28 (**8**): 084209. DOI: 10.1088/1674-1056/28/8/084209

Monolithic all-fiber mid-infrared supercontinuum source based on a step-index two-mode As_2S_3 fiber

Jinmei Yao(姚金妹), Bin Zhang(张斌), Jing Hou(侯静)

Chin. Phys. B, 2019, 28 (**6**): 064205. DOI: 10.1088/1674-1056/28/6/064205

Mid-infrared supercontinuum and optical frequency comb generations in a multimode tellurite photonic crystal fiber*

Xu Han(韩旭)[1], Ying Han(韩颖)[1,†], Chao Mei(梅超)[2], Jing-Zhao Guan(管景昭)[1], Yan Wang(王彦)[1], Lin Gong(龚琳)[1], Jin-Hui Yuan(苑金辉)[2], and Chong-Xiu Yu(余重秀)[2]

[1] *Key Laboratory for Special Fiber and Fiber Sensor of Hebei Province, School of Information Science and Engineering, Yanshan University, Qinhuangdao* 066004, *China*

[2] *State Key Laboratory of Information Photonics and Optical Communications, Beijing University of Posts and Telecommunications (BUPT), Beijing* 100876, *China*

(Received 6 January 2021; revised manuscript received 18 March 2021; accepted manuscript online 23 March 2021)

We numerically investigate the mid-infrared (MIR) supercontinuum (SC) and SC-based optical frequency comb (OFC) generations when the three optical modes (LP_{01}, LP_{02}, and LP_{12}) are considered in a multimode tellurite photonic crystal fiber (MM-TPCF). The geometrical parameters of the MM-TPCF are optimized to support the multimode propagation and obtain the desired dispersion characteristics of the considered three optical modes. When the pump pulse with center wavelength $\lambda = 2.5$ μm, width $T = 80$ fs, and peak power $P = 18$ kW is coupled into the anomalous dispersion region of the LP_{01}, LP_{02}, and LP_{12} modes of the MM-TPCF, the −40-dB bandwidth of the generated MIR SCs can be up to 2.56, 1.39, and 1.12 octaves, respectively, along with good coherence. Moreover, the nonlinear dynamics of the generated SCs are analyzed. Finally, the MIR SCs-based OFCs are demonstrated when a train of 50 pulses at 1-GHz repetition rate is used as the pump source and launched into the MM-TPCF.

Keywords: multimode tellurite photonic crystal fiber, supercontinuum, optical frequency comb, mid-infrared spectral region

PACS: 42.65.Wi, 42.65.Re, 42.70.Km **DOI:** 10.1088/1674-1056/abf10f

1. Introduction

Supercontinuum (SC) in the mid-infrared (MIR) spectral region has extensive applications in optical frequency comb (OFC),[1] spectroscopy,[2] optical coherence tomography,[3] and optical communication.[4] When the short pulse propagates in the nonlinear medium, the SC could be generated from the interplay of some nonlinear effects, including stimulated Raman scattering (SRS), self-phase modulation (SPM), four-wave mixing (FWM), modulation instability (MI), and soliton fission (SF).[5–10] Photonic crystal fiber (PCF) is considered as one of the excellent nonlinear media for the SC generation due to its excellent optical properties such as adjustable dispersion, enhanced nonlinearity, high birefringence, *etc.*[5,11,12] In 2002, Dudley *et al.*[13] firstly reported the SC generation in the silica PCFs by using the short pulses as the pump source. Since then, there are lots of reports on the SC generation in the silica PCFs.[14–18] In recent years, some novel PCFs, which are fabricated from the fluoride, chalcogenide, and tellurite glasses are demonstrated. Compared with the silica glass, these glasses have lower transmission loss in the MIR spectral region and higher nonlinear refractive index n_2, so they can be used as the materials of the PCF for investigating the nonlinear effects.[19,20] Among them, n_2 of the tellurite glass is one order of magnitude larger than that of the silica glass. In addition, it is chemically and thermally stable compared with the fluoride and chalcogenide glasses.[21,22] Therefore, the tellurite glass has been considering as the ideal nonlinear medium for the MIR SC generation. In 2008, Domachuk *et al.*[22] reported the SC generation spanning from 0.79 μm to 4.9 μm in a tellurite PCF. In 2016, Ou *et al.*[23] obtained the MIR SC spanning from 1.8 μm to 14 μm by using a highly nonlinear Ge–Sb–Se fiber. In 2017, Zhao *et al.*[24] demonstrated the MIR SC generation covering 2 μm–16 μm in a low-loss telluride single-mode fiber. In 2017, Li *et al.*[25] demonstrated the highly coherent and octave-spanning MIR SC generation in a tellurite PCF. In 2018, we investigated the self-similar pulse compression and its application in the MIR SC generation in the tellurite PCFs.[26] In 2019, Nguyen *et al.*[27] obtained a highly coherent SC spanning from 1.4 μm to 3 μm in a microstructured tellurite fiber pumped by a laser operating at 2 μm. In the same year, Klimczak *et al.*[28] obtained the SC with a spectral width covering wavelengths of 1100 nm–2600 nm centered at 1560 nm using a highly nonlinear tellurite glass PCF.

Until now, most of investigations are concentrated on the

*Project supported by the National Natural Science Foundation of China (Grant Nos. 12074331, 61875238, and 61971373), the Natural Science Foundation of Hebei Province, China (Grant Nos. F2021203002, F2019203549, and F2020203050), and the Science and Technology Support Projects of Research and Development Plans of Qinhuangdao City (Grant No. 202004A001).

†Corresponding author. E-mail: hanyingysu@163.com

© 2021 Chinese Physical Society and IOP Publishing Ltd

SC generation based on the fundamental mode of the PCFs. As the fiber laser and optical communication technologies develop rapidly, the multimode nonlinear fiber optics has been attracting great research interests.[29–31] Recently, the SC generations based on the high-order modes in the multimode PCFs have already been reported. In 2008, Cherif *et al.*[32] reported the SC generation when the femtosecond pump pulses are coupled into the LP_{11} and LP_{21} modes of a silica PCF. In 2013, Chen *et al.*[33] demonstrated the SC generation from the visible to ultraviolet spectral region by coupling the sub-ns pulses at wavelength 532 nm into the LP_{02} mode of a silica PCF. In 2016, Jiang *et al.*[34] experimentally generated the MIR SC when the pump pulses are launched into the fundamental and first higher-order modes of a ZBLAN PCF. In the same year, Kubat *et al.*[35] obtained the MIR SC when several higher-order modes are excited in a chalcogenide PCF. In 2018, Khalifa *et al.*[36] obtained a mid-infrared supercontinuum spanning 2 μm to 4 μm at −40 dB for mode HE_{11} from 2 μm to 3.5 μm for HE_{12} using a multimode As_2S_3 PCF. In 2020, Eslami *et al.*[37] demonstrated the generation of a low-noise, octavespanning mid-infrared supercontinuum from 1700 nm to 4800 nm using a multimode step-index chalcogenide fiber with the higher-order modes. At present, there is still no report on the SC generation in the higher-order modes of the multimode tellurite PCF (MM-TPCF).

In this paper, the highly coherent and octave-spanning MIR SCs are generated when the femtosecond pump pulses are coupled into the anomalous dispersion region of the LP_{01}, LP_{02}, and LP_{12} modes of the designed MM-TPCF. The influences of the pump pulse parameters including center wavelength, width, and peak power on the SC generations are investigated. The temporal and spectral evolutions of the SC generation for the three optical modes are demonstrated. Finally, the SC-based OFCs are obtained when a train of 50 pulses at 1 GHz repetition rate is used as the pump source.

2. Theoretical model and design of the MM-TPCF

Figure 1(a) shows the cross-section of the designed MM-TPCF, where the four rings of air-holes are arranged in a regular hexagonal lattice, the core diameter D is 4.6 μm, hole to hole pitch Λ is 15 μm, and air hole diameter d is 0.7Λ. The single-mode propagation condition of the MM-TPCF can be described as follows:

$$V=\frac{2\pi a}{\lambda}(n_1^2-n_2^2)^{1/2}<2.405, \tag{1}$$

where V is the normalized frequency, a is the core radius, λ is the wavelength of the propagated light, and n_1 and n_2 are the effective refractive indices of the core and cladding regions, respectively. When $V=2.405$, the corresponding cut-off wavelength $\lambda_{\text{cut-off}}$ can be obtained by Eq. (1). When the pump wavelength is larger than $\lambda_{\text{cut-off}}$, the single-mode propagation can be achieved. When the pump wavelength is smaller than $\lambda_{\text{cut-off}}$, the MM-TPCF supports the multimode propagation. According to Eq. (1), V is dependent on n_1 and n_2. In order to ensure the multimode propagation, two kinds of materials, which have the large effective refractive index difference, need to be carefully chosen as the core and cladding materials to increase $\lambda_{\text{cut-off}}$. The chosen materials should have the similar thermal expansion and softening temperatures, which is necessary for the actual fabrication of the MM-TPCF. Thus, TLWMN (TeO_2–Li_2O–WO_3–MoO_3–Nb_2O_3) and TZLKAP (TeO_2–ZnO–Li_2O–K_2O–Al_2O_3–P_2O_5) are used as the core and cladding materials, respectively.[38–40] In practice, the designed MM-TPCF can be fabricated with the stack-and-draw technique. We use the full-vector finite element method (FV-FEM) to calculate the propagation characteristics of the designed MM-TPCF. In the calculation, the perfectly matched layer (PML), whose thickness and refractive index are set as 10 μm and $n_{\text{silica}}+0.03$, is used as the boundary condition. In addition, the grid sizes of the silica, air holes, and PML are set as $\lambda/4$, and the grid size of the core region filled with the nitrobenzene is set as $\lambda/6$. With the FV-FEM, the mode field distributions of the considered LP_{01}, LP_{02}, and LP_{12} modes calculated at wavelength 3 μm are shown in Figs. 1(b), 1(c), and 1(d), respectively. From Figs. 1(b), 1(c), and 1(d), the mode field energy can be well confined in the core region of the MM-TPCF, which consists of the TLWMN material and is marked by the circle.

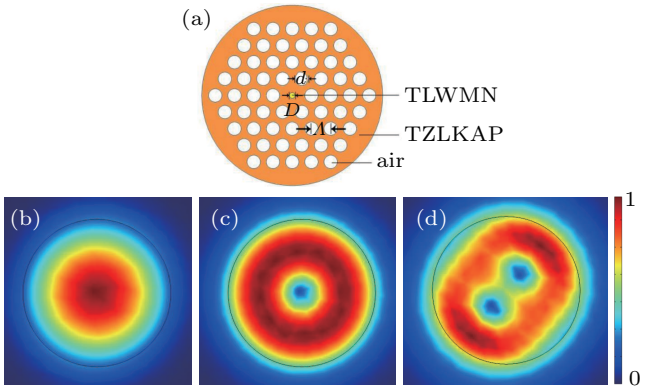


Fig. 1. (a) The cross-section of the designed MM-TPCF. Mode field distributions of (b) LP_{01} mode, (c) LP_{02} mode, and (d) LP_{12} mode calculated at wavelength 3 μm.

The curves of the effective refractive index N_{eff} and effective mode field area A_{eff} calculated as functions of the wavelength for the three optical modes are shown in Fig. 2(a). From Fig. 2(a), compared with the LP_{01} mode, N_{eff} and A_{eff} of the

LP_{02} and LP_{12} modes decrease and increase faster as the wavelength increases, respectively. The group-velocity dispersion parameter D can be derived from $N_{\rm eff}$ as follows:

$$D = -\frac{\lambda}{c}\frac{{\rm d}^2 N_{\rm eff}}{{\rm d}\lambda^2}, \tag{2}$$

where c is the light velocity in the vacuum. Figure 2(b) shows the D and nonlinear coefficients γ of the LP_{01}, LP_{02}, and LP_{12} modes of the MM-TPCF. From Fig. 2(b), the three optical modes show the anomalous dispersion characteristic at the initial pump wavelength 2 μm. The first zero-dispersion wavelengths (ZDWs) of the LP_{01}, LP_{02}, and LP_{12} modes are located at wavelengths 1.72, 1.48, and 1.28 μm, respectively. The second ZDWs of the LP_{12} mode is located at wavelength 4.58 μm. γ can be calculated from $A_{\rm eff}$, which is related to the integration on the whole cross-section of the MM-TPCF as

$$\begin{aligned}\gamma &= \frac{2\pi n_2}{\lambda A_{\rm eff}} \\ &= \frac{2\pi}{\lambda}\frac{\iint n_2(x,y)\,|F(x,y)|^4\,{\rm d}x{\rm d}y}{\iint |F(x,y)|^2\,{\rm d}x{\rm d}y},\end{aligned} \tag{3}$$

where $F(x,y)$ is the distribution of the mode fields and $n_2 = 5.9\times10^{-19}$ m^2/W is the nonlinear refractive index of TL-WMN. From Fig. 2(b), γ of the LP_{01} mode is much larger than those of the LP_{02} and LP_{12} modes, and γ curves of the LP_{02} and LP_{12} modes are nearly overlapped, which means that they have the similar nonlinearity.

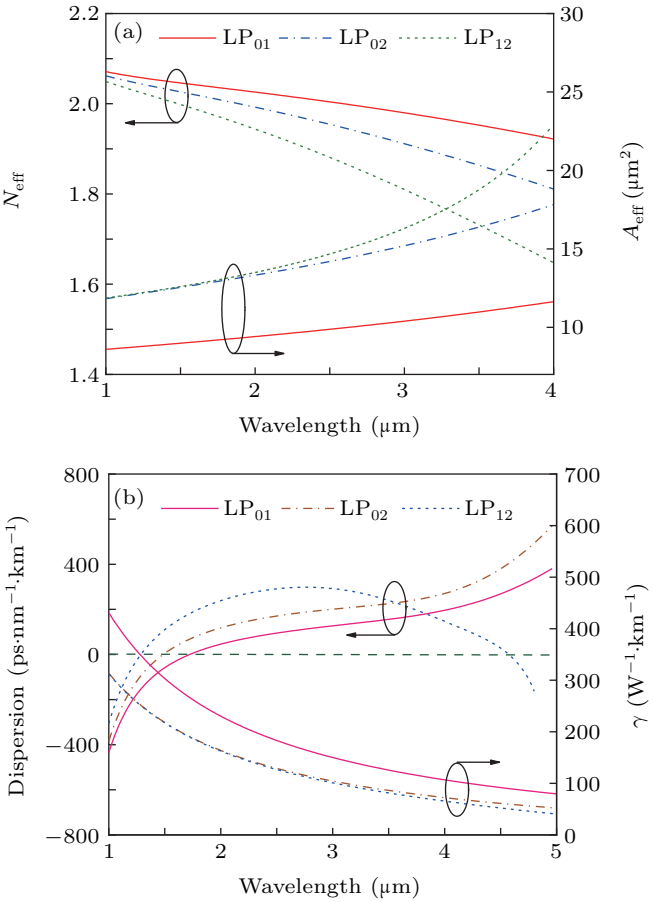


Fig. 2. (a) The effective refractive index $N_{\rm eff}$ and effective mode field area $A_{\rm eff}$ calculated for the LP_{01}, LP_{02}, and LP_{12} modes, respectively. (b) Group-velocity dispersion parameter D and nonlinear coefficient γ calculated for the LP_{01}, LP_{02}, and LP_{12} modes, respectively.

The nonlinear dynamics of the short pulse propagated in the designed MM-TPCF can be modelled by the following generalized nonlinear Schrödinger equation (GNLSE)[5,12]

$$\begin{aligned}&\frac{\partial A}{\partial z} + \frac{\alpha_0}{2}A - \sum_{m\geq 2}\frac{{\rm i}^{m+1}\beta_m}{m!}\frac{\partial^m A}{\partial t^m} \\ &= {\rm i}\gamma\times\left(1+\tau_{\rm shock}\frac{\partial}{\partial t}\right) \\ &\quad\times\left[A(z,t)\int_0^\infty R(t')\,|A(z,t-t')|^2\,{\rm d}t'\right],\end{aligned} \tag{4}$$

where $A(z,t)$ represents the slowly varying envelope during the propagation, α is the linear propagation loss, β_m means the m-order dispersion coefficient calculated from the Taylor expansion of the propagation constant $\beta(\omega)$ at a specific wavelength, and γ is the nonlinear coefficient. Nonlinear dispersion $\tau_{\rm shock} = \gamma_1(\omega_0)/\gamma(\omega_0)$ corresponds to the effect of self-steeping (SS), where $\gamma_1(\omega) = {\rm d}\gamma(\omega)/{\rm d}\omega$ and ω is the central angular frequency. $R(t)$ denote the nonlinear response function, which can be described as

$$R(t) = (1-f_{\rm R})\delta(t) + f_{\rm R}h_{\rm R}(t), \tag{5}$$

where $f_{\rm R}$ is the fractional contribution of the Raman response, and $\delta(t)$ represents the Kerr effect. The delayed Raman response function $h_{\rm R}(t)$ is described as

$$h_{\rm R}(t) = \frac{\tau_1^2+\tau_2^2}{\tau_1\tau_2^2}\exp\left(-\frac{t}{\tau_2}\right)\sin\left(\frac{t}{\tau_1}\right), \tag{6}$$

where τ_1 is the Raman period corresponding to the phonon oscillation frequency, and τ_2 is the spectral bandwidth of the Raman gain. Some parameters used in the simulation are listed in Table 1.[39]

Table 1. Some parameters used in the simulation.

Parameters	PCF length (mm)	$f_{\rm R}$	τ_1 (fs)	τ_2 (fs)
Value	3	0.064	7.4413	46.932

The coherence is one of the important parameters to evaluate the quality of the SC generated. The following three parameters can be used to quantify the coherence of the SC[41,42]

$$g_{1,2}^{(1)}(\lambda, t_1-t_2) = \left|\frac{\langle A_1^*(\lambda,t_1)A_2(\lambda,t_2)\rangle}{\left\langle|A_1(\lambda,t_1)|^2\right\rangle\left\langle|A_2(\lambda,t_2)|^2\right\rangle}\right|, \tag{7}$$

$$R = \frac{\int_0^\infty g_{12}^{(1)}(\lambda,t_1-t_2)P(\lambda,t_1-t_2)\,{\rm d}\lambda}{\int_0^\infty P(\lambda,t_1-t_2)\,{\rm d}\lambda}, \tag{8}$$

$$K = \lg(1-R), \tag{9}$$

where $g_{1,2}^{(1)}$ is the first-order degree of coherence, indicating the correlation of the signals from shot-to-shot at wavelength λ for $t_1 = t_2$. $A(\lambda,t)$ is the signal spectral amplitude with the random noise. $n = \eta N \exp(\mathrm{i}2\pi U)$ represents for the noise seed, where η is the noise level representing the degree of noise in relation to the pulse, N is a random variable with the standard normal distribution, and U is a random variable with the uniform distribution between 0 to 1. The angular brackets denote the ensemble average among the independent pairs of the generated spectra. Here, 50 shots with different random noise seeds are used to calculate Eq. (7). The weighted degree of coherence R in Eq. (8) measures the averaged coherence in the whole spectrum, where $P(\lambda,t) = \left\langle |A(\lambda,t)|^2 \right\rangle$ denotes the ensemble average intensity of the generated spectra. In Eq. (9), K is used to compare the tiny difference of the high coherence.

3. Simulation results and discussion

We use the fourth-order Runge–Kutta method to solve the GNLSE for investigating the nonlinear dynamics of the SC generation.[40] The hyperbolic secant pulses with different parameters are used as the pump source and coupled into the LP_{01}, LP_{02}, and LP_{12} modes of the designed MM-TPCF with the length of 3 mm, respectively. In the simulation, the 12th-order dispersion coefficient is considered, as shown in Table 2. In the following, we will investigate the influences of the pump pulse parameters on the SC generation.

Table 1. The dispersion coefficient β_m calculated at wavelength 2.5 μm.

m	β_m		
	LP_{01}	LP_{02}	LP_{12}
2	-2.98×10^{-1} (ps^2/m)	-5.33×10^{-1} (ps^2/m)	-1.02 ps^2/m
3	1.69×10^{-3} (ps^3/m)	2.39×10^{-3} (ps^3/m)	3.35×10^{-3} (ps^3/m)
4	-1.30×10^{-5} (ps^4/m)	-2.02×10^{-5} (ps^4/m)	8.28×10^{-6} (ps^4/m)
5	6.26×10^{-8} (ps^5/m)	7.75×10^{-8} (ps^5/m)	-1.58×10^{-7} (ps^5/m)
6	1.15×10^{-9} (ps^6/m)	2.71×10^{-9} (ps^6/m)	-2.51×10^{-9} (ps^6/m)
7	-1.20×10^{-11} (ps^7/m)	-2.89×10^{-11} (ps^7/m)	4.68×10^{-11} (ps^7/m)
8	-3.22×10^{-13} (ps^8/m)	-5.65×10^{-13} (ps^8/m)	3.90×10^{-13} (ps^8/m)
9	8.98×10^{-15} (ps^9/m)	1.69×10^{-14} (ps^9/m)	-1.80×10^{-14} (ps^9/m)
10	-9.91×10^{-17} (ps^{10}/m)	-1.89×10^{-16} (ps^{10}/m)	2.21×10^{-16} (ps^{10}/m)
11	5.57×10^{-19} (ps^{11}/m)	1.07×10^{-18} (ps^{11}/m)	-1.31×10^{-18} (ps^{11}/m)
12	-1.33×10^{-21} (ps^{12}/m)	-2.56×10^{-21} (ps^{12}/m)	3.22×10^{-21} (ps^{12}/m)

Figures 3(a)–3(f) show the temporal and spectral profiles of the generated SC when the pump pulse with width $T = 80$ fs, peak power $P = 18$ kW, and center wavelength $\lambda = 2.0$, 2.5, 3.0, and 3.5 μm are coupled into the anomalous dispersion region of the LP_{01}, LP_{02}, and LP_{12} modes of the 3-mm-long MM-TPCF, respectively. In Figs. 3(a) and 3(b), when the pump pulse at $\lambda = 2.0$, 2.5, 3.0, and 3.5 μm are coupled into the LP_{01} mode, the soliton dynamics dominate the nonlinear process. From Fig. 3(a), several small peaks can be observed, corresponding to the lower-order solitons. In addition, because of the intrapulse Raman scattering effect, the fundamental solitons formed by the higher-order soliton occur to red-shift and separate after a short propagation distance. With the increase of λ, the satellite separates to the right side due to the SF effect. Moreover, because of the higher-order dispersions and resonance matching condition, the blue-shifted dispersive waves (DWs) are generated at the short wavelength side. After that, the cross-phase modulation (XPM) effect between the red-shifted solitons and DWs could further expand the optical spectra toward the longer and shorter wavelength sides. From Fig. 3(b), when $\lambda = 2.5$ μm, the −40-dB bandwidth of the SC generated spans from 0.9 μm to 5.3 μm, covering 2.56 octaves. It is worth noting that when λ is further increased to 3.0 μm and 3.5 μm, the optical spectra become narrower. The main reason may be due to the increasing dispersion and decreasing nonlinearity. Figures 3(c) and 3(d) show the spectral and temporal profiles of the SCs generated with the LP_{02} mode. Compared with the results shown in Figs. 3(a) and 3(b), although the nonlinear process is similar, the spectral and temporal profiles are different. It can be seen from Figs. 3(c) and 3(d) that the −40-dB bandwidth of the SC generated spans from 1.6 μm to 4.2 μm, covering 1.39 octaves, when $\lambda = 2.5$ μm. The bandwidth is much smaller than that obtained with the LP_{01} mode, especially for $\lambda = 2.0$ μm and 2.5 μm. The main reason is considered that γ of the LP_{02} mode is reduced obviously. Figures 3(e) and 3(f) show the spectral and temporal profiles of the SCs generated with the LP_{02} mode. From Figs. 3(e) and 3(f), the spectral and temporal profiles are similar to that obtained with the LP_{02} mode because of the similar nonlinear process and γ. When $\lambda = 2.5$ μm, the −40-dB bandwidth of the SC generated spans from 1.8 μm to 3.9 μm, covering 1.12 octaves. Thus, when $\lambda = 2.5$ μm,

the octave-spanning SCs can be generated with the considered three optical modes.

Figures 4(a)–4(f) show the temporal and spectral profiles of the generated SC when the pump pulse with $\lambda_0 = 2.5$ μm, $P = 18$ kW, and $T = 80$, 120, 150, and 200 fs is coupled into the anomalous dispersion region of the LP_{01}, LP_{02}, and LP_{12} modes of the 3-mm-long MM-TPCF, respectively. From the temporal profiles of the SCs for the three optical modes shown in Figs. 4(a), 4(c), and 4(e), the temporal width becomes larger as T increases, and several small peaks induced by the SF effect emerge for the narrower pulse. The soliton order N can be calculated by

$$N^2 = \frac{\gamma T_0^2 P_0}{|\beta_2|}. \tag{10}$$

From Eq. (10), N is related to T, P, γ, and the 2nd-order dispersion coefficient β_2. Because N is proportional to T, N becomes larger as T_0 increases. From the spectral profiles of the SCs for the three optical modes shown in Figs. 4(b), 4(d), and 4(f), when $T = 80$ fs and 120 fs, the optical spectra are asymmetrically broadened by the SF and XPM effects. Especially for $T = 80$ fs, the −40-dB bandwidths of the SCs generated for the LP_{01}, LP_{02}, and LP_{12} modes span from 0.9 μm to 5.3 μm, 1.6 μm to 4.2 μm, and 1.8 μm to 3.9 μm, covering 2.56, 1.39, and 1.12 octaves, respectively. When $T = 150$ fs and 200 fs, the optical spectra are symmetrically broadened, and the spectral bandwidths become narrower. In addition, the coherence of the SC could be obviously degraded by the MI effect when T is larger. Thus, $T = 80$ fs is chosen as optimized value.

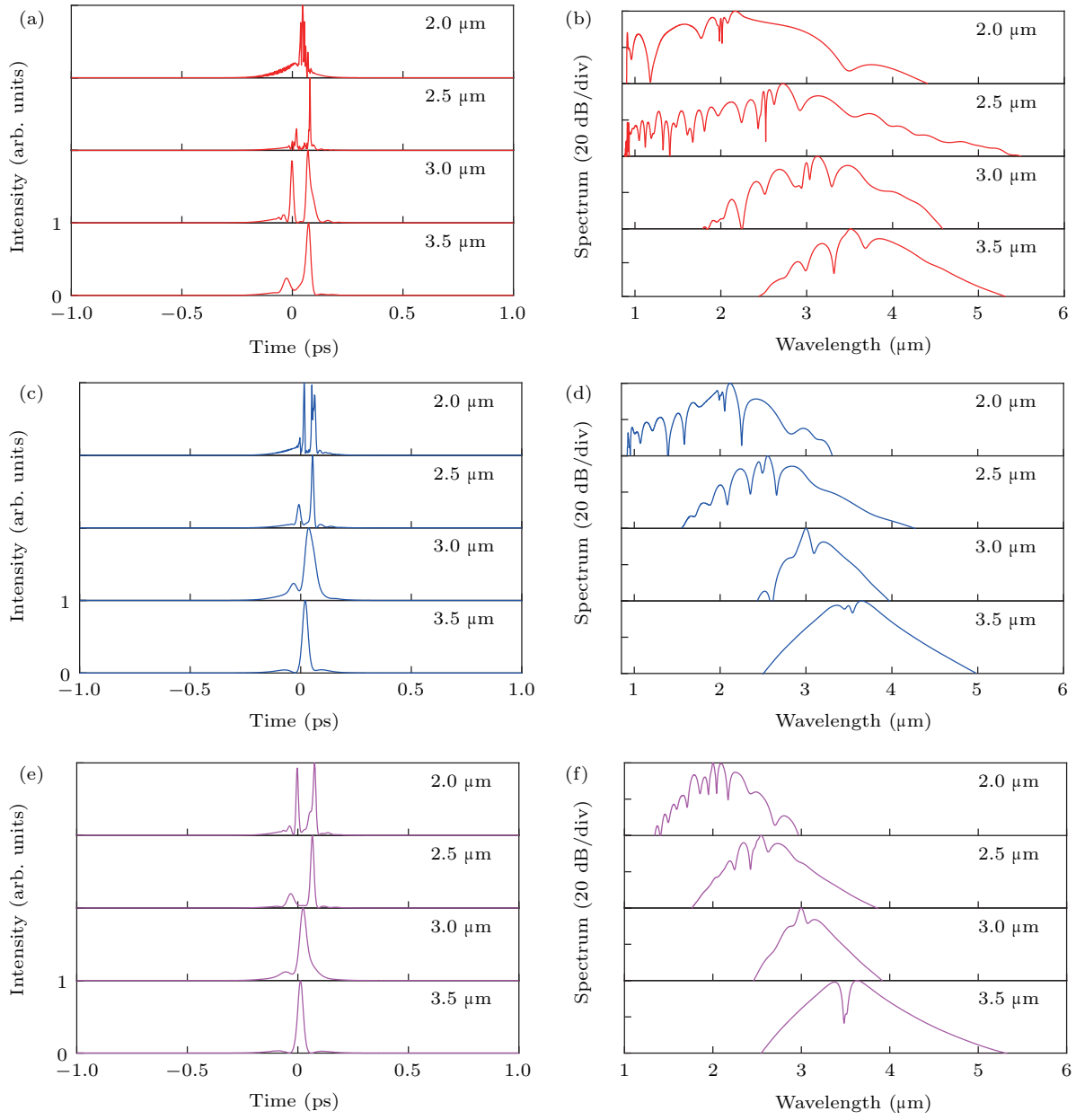


Fig. 3. The temporal (panels (a), (c), (e)) and spectral (panels (b), (d), (f)) profiles of the SC generated when pump pulse with width $T = 80$ fs, peak power $P = 18$ kW, and center wavelength of $\lambda = 2.0$, 2.5, 3.0, and 3.5 μm is coupled into (a) LP_{01}, (b) LP_{02}, and (c) LP_{12} modes of the MM-TPCF, respectively.

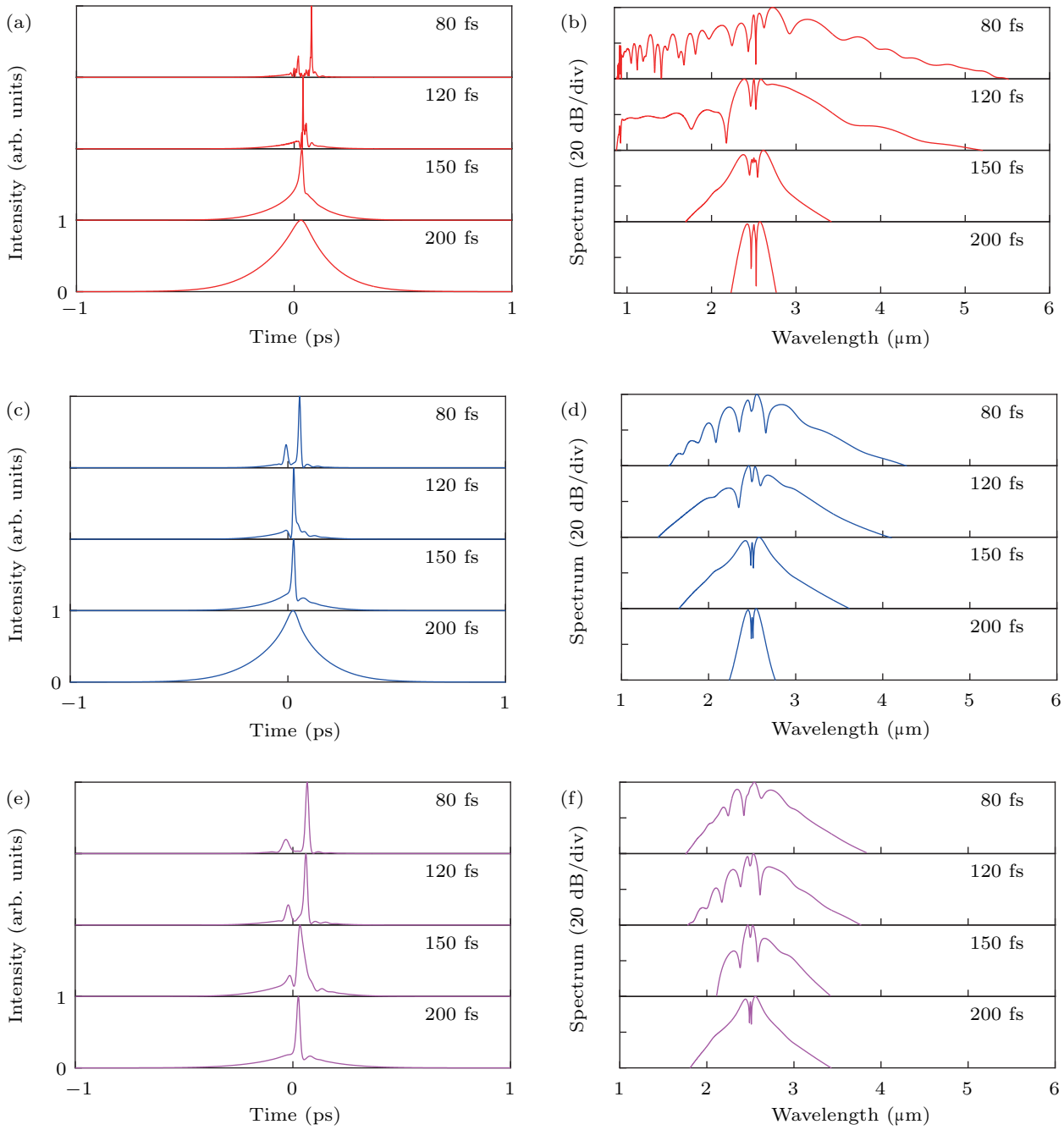


Fig. 4. The temporal (panels (a), (c), (e)) and spectral (panels (b), (d), (f)) profiles of the SC generated when pump pulse with $\lambda = 2.5$ μm, $P = 18$ kW, and $T = 80$, 120, 150, and 200 fs is coupled into (a) LP_{01}, (b) LP_{02}, and (c) LP_{12} modes of the MM-TPCF, respectively.

Figures 5(a)–5(f) show the temporal and spectral profiles of the generated SC when the pump pulse with $\lambda = 2.5$ μm, $T = 80$ fs, and $P = 12$, 15, 18, and 25 kW is coupled into the anomalous dispersion region of the LP_{01}, LP_{02}, and LP_{12} modes of the 3-mm-long MM-TPCF, respectively. When T_0 is fixed, the spectral broadening mainly depends on P. Thus, as P_0 increases, the optical spectra can be obviously broadened by the SF and XPM effects. From the temporal profiles of the SCs for the three optical modes shown in Figs. 5(a), 5(c), and 5(e), as P_0 increases, N increases, and the spectrum becomes broader gradually. Several small peaks along with some burrs emerge, and they separate to the right side due to the enhanced SF effect. From the spectral profiles of the SCs for the three optical modes shown in Figs. 5(b), 5(d), and 5(f), as P_0 increases, the spectral broadening increases gradually due to the combined effect of the MI, SF, and XPM, and some dips emerge because of the degradation of the coherence with the increase of N. When $P = 18$ kW, the −40-dB bandwidths of the SCs generated for the LP_{01}, LP_{02}, and LP_{12} modes span from 0.9 μm to 5.3 μm, 1.6 μm to 4.2 μm, and 1.8 μm to 3.9 μm, covering 2.56, 1.39, and 1.12 octaves, respectively. It is worth indicating that when P is further increased to 25 kW, the optical spectrum does not broaden any more. Thus, $P = 18$ kW is chosen as the optimized value.

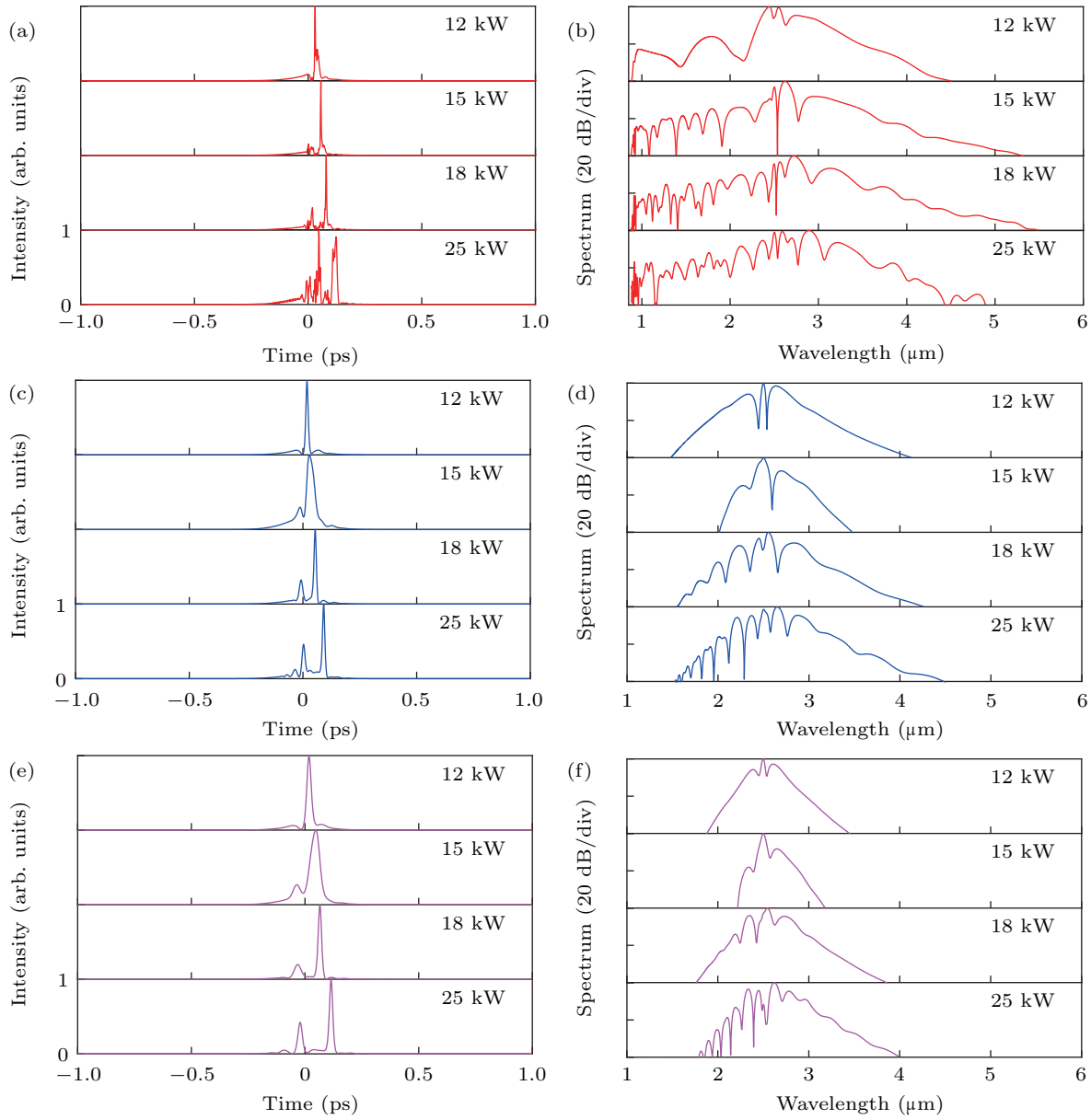


Fig. 5. The temporal (panels (a), (c), (e)) and spectral (panels (b), (d), (f)) profiles of the SC generated when pump pulse with $\lambda = 2.5$ μm, $T = 80$ fs, and $P = 12$, 15, 18, and 25 kW is coupled into (a) LP_{01}, (b) LP_{02}, and (c) LP_{12} modes of the MM-TPCF, respectively.

Based on the above discussion, the optimized pump pulse parameters are chosen as following: $\lambda = 2.5$ μm, $T = 80$ fs, and $P = 18$ kW. When the pump pulse with these parameters is coupled into the anomalous dispersion region of the LP_{01}, LP_{02}, and LP_{12} modes of the 3-mm-long MM-TPCF, respectively, the temporal and spectral evolutions of the LP_{01}, LP_{02}, and LP_{12} modes are shown in Figs. 6(a)–6(f). During the propagation, the pump pulse experiences the anomalous dispersion, so the SF and XPM effects play important roles in the SC generation. From the temporal evolution diagrams of the SCs for the three optical modes shown in Figs. 6(a), 6(c), and 6(e), with the increase of the propagation length z, the pump pulse is first compressed and then broadened. At the output end of the MM-TPCF, several small peaks emerge, and they separate to the right side because of the SF effect. From the spectral evolution diagrams of the SCs for the three optical modes shown in Figs. 6(b), 6(d), and 6(f), the solitons start to separate at $z = 2$ mm, and the optical spectrum is broadened quickly. After that, the XPM-induced spectral broadening further expands the optical spectrum at the short and long wavelength sides as z increases. Some dips are observed from the optical spectra at the output end of the MM-TPCF because of the degradation of the coherence. For $T = 80$ fs, the MI effect is depressed, and the degradation of the coherence could be resulted from the noise induced by the SF effect. After the 3-mm propagation in the MM-TPCF, the highly coherent and octave-spanning MIR SCs can be generated for the LP_{01}, LP_{02}, and LP_{12} modes in the wavelength ranges of 0.9 μm to 5.3 μm, 1.6 μm to 4.2 μm, and 1.8 μm to 3.9 μm, covering 2.56, 1.39, and 1.12 octaves, respectively.

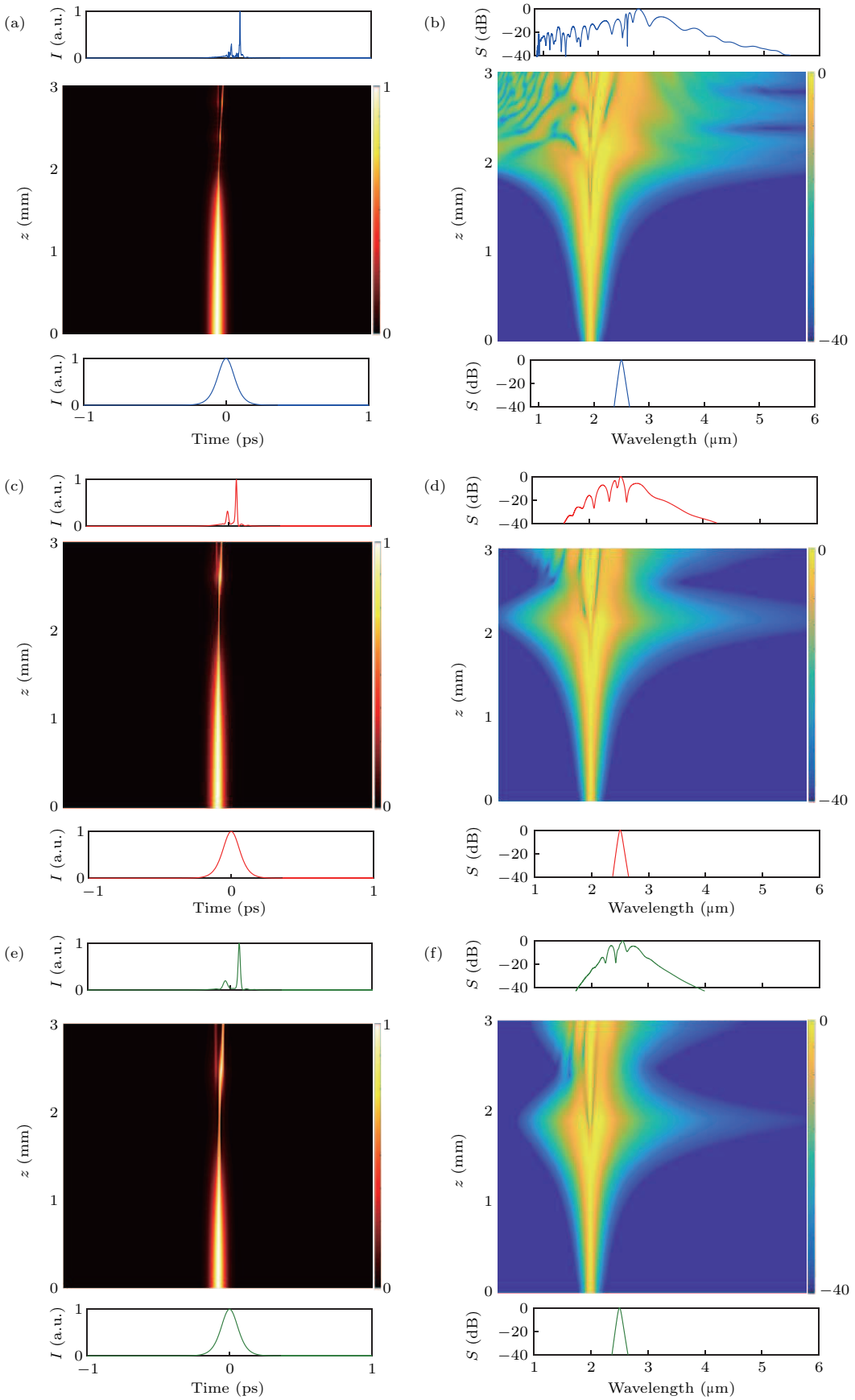


Fig. 6. When the pump pulse with $\lambda = 2.5$ μm, $T = 80$ fs, and $P = 18$ kW are used, the temporal (panels (a), (c), (e)) and spectral (panels (b), (d), (f)) evolutions of the pump pulses along the propagation length z for (a) LP_{01}, (b) LP_{02}, and (c) LP_{12} modes. The temporal and spectral profiles at the input and output of the MM-TPCF are also shown at the bottom and top of the evolution diagrams. The unit a.u. is the abbreviation of arbitrary unit.

In the following, we will analyze the influence of the random noise on the MIR SC generation. We use the 50 shots of optical pulses with $\eta = 0.001$ as the pump source. Figures 7(a), 7(b), and 7(c) show the MIR SC generated and coherence of the LP_{01}, LP_{02}, and LP_{12} modes for different η, respectively. The gray lines are the overlapped spectra of 50 shots with the random noise. From Fig. 7(a), the MIR SCs of 50 shots pulses differs obviously in the wavelength range of less than 2 μm, and the corresponding coherence of the SC is very unstable. In contrast, the red curve almost overlaps with the gray curve in the wavelength range of larger than 2 μm, and the coherence of the SC is very close to 1. From Figs. 7(b) and 7(c), the blue, magenta, and gray curves for the LP_{02} and LP_{12} modes almost completely overlap. Thus, the coherences of the SC are maintained 1. It is worth indicating that although the pump pulse works in the anomalous dispersion region of the LP_{01}, LP_{02}, and LP_{12} modes of the MM-TPCF, the MIR SC with good coherence could be generated since the pulse with $T = 80$ fs is used as the pump source and the noise amplification induced by the MI effect can be depressed.

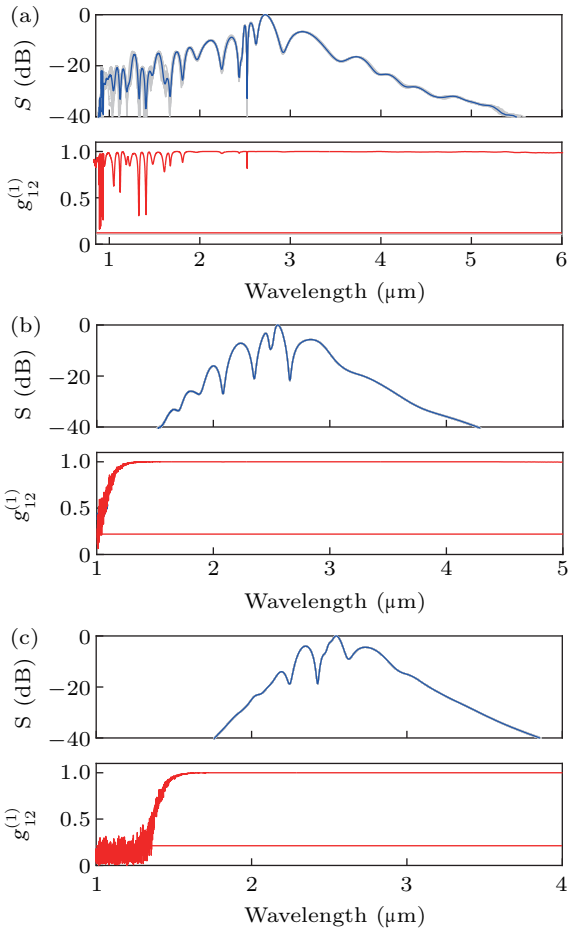


Fig. 7. The generated SCs at the top and $g_{1,2}^{(1)}$ at the bottom with a noise level $\eta = 0.001$ for (a) LP_{01}, (b) LP_{02}, and (c) LP_{12} modes. The grey lines are the overlapped spectra of the 50 shots with the random noise. The red, blue, and magenta lines represent the averaged spectra of the 50 shots, respectively.

To obtain the quantitative result of the coherence of the MIR SC in the considered wavelength range, η is chosen in the range from 10^{-6} to 10^{-1}, and 50 shots pulses are still used as the pump source. After the coherence is obtained, R is calculated according to Eq. (8), and the curve of R with respect to $\lg(\eta)$ is shown in Fig. 8(a). It can be seen from Fig. 8(a) that when $\lg(\eta) \leq -3$, R of the LP_{01}, LP_{02}, and LP_{12} modes is close to 1, which means that the SCs generated with the three optical modes have good coherence. When $\lg(\eta)$ increases to -2, R of the LP_{01} mode drops rapidly to 0.59, while R of the LP_{02} and LP_{12} modes is still approximately 1. As $\lg(\eta)$ continues to increase, R of the LP_{01} mode drops to 0.38, and R of the LP_{02} and LP_{12} modes both fall below 0.9. Since R of the three optical modes are very close to 1 when $\lg(\eta) \leq -3$, the curve of K with respect to $\lg(\eta)$ is calculated by Eq. (9), as shown in Fig. 8(b). The three increasing curves indicate that as $\lg(\eta)$ increases, the coherence is degraded. From Fig. 8(b), the coherence of the LP_{02} mode is better than that of the LP_{12} mode when $\lg(\eta) \leq -3$, and the coherence of the LP_{12} mode is better than that of the LP_{02} mode when $\lg(\eta) > -3$. Compared with the LP_{01} mode, when $\lg(\eta) = -6$, the coherence of the LP_{01} mode is between the LP_{02} and LP_{12} modes. When $\lg(\eta) = -5$, the coherence of the LP_{01} mode is almost the

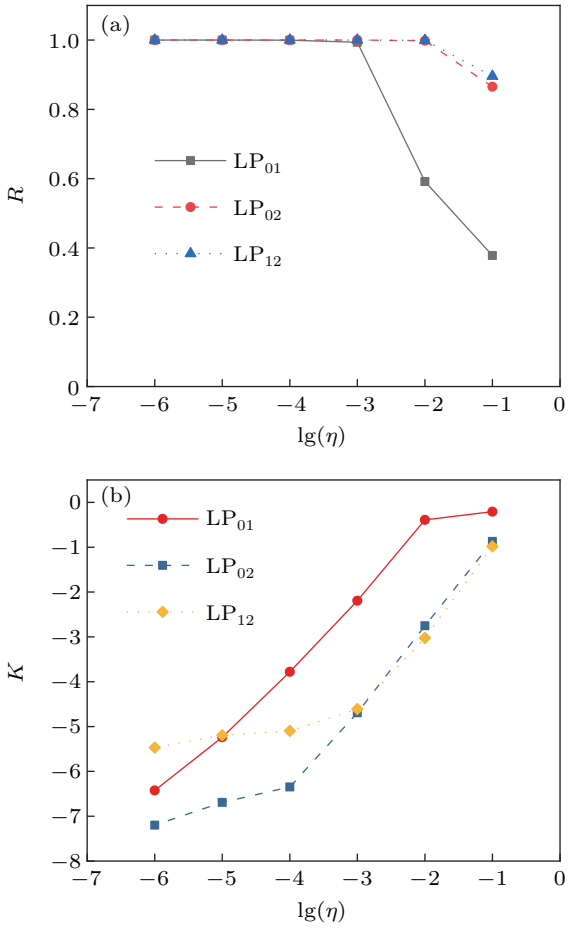


Fig. 8. (a) R and (b) K as functions of $\lg(\eta)$ for the LP_{01}, LP_{02}, and LP_{12} modes, respectively.

same as the LP_{02} mode. When $\lg(\eta) \geq -4$, the coherence of the LP_{01} mode degrades rapidly, which is much worse than the other two optical modes.

In order to obtain the SC-based OFC source, we launch a train of 50 pulses at a repetition rate of 1 GHz into the anomalous dispersion region of the LP_{01}, LP_{02}, and LP_{12} modes of the designed MM-TPCF. The OFCs generated with the LP_{01}, LP_{02}, and LP_{12} modes are shown in Figs. 9(a), 9(b), and 9(c), respectively, where the shaded color regions represent the highly dense OFCs. To observe the individual comb lines clearly, the zoom-in views of the OFCs generated at 100 THz (upper) and 120 THz (lower) are shown in the inserts of Figs. 9(a), 9(b), and 9(c). It can be seen from the insets of Figs. 9(a), 9(b), and 9(c) that the discrete comb line has a frequency interval of 1 GHz, and the comb line amplitude in the sampling bandwidth of 5 GHz is equal. Among them, because the coherence of the SC generated with the LP_{01} mode is not very good, each comb line of the LP_{01} mode shows asymmetric.

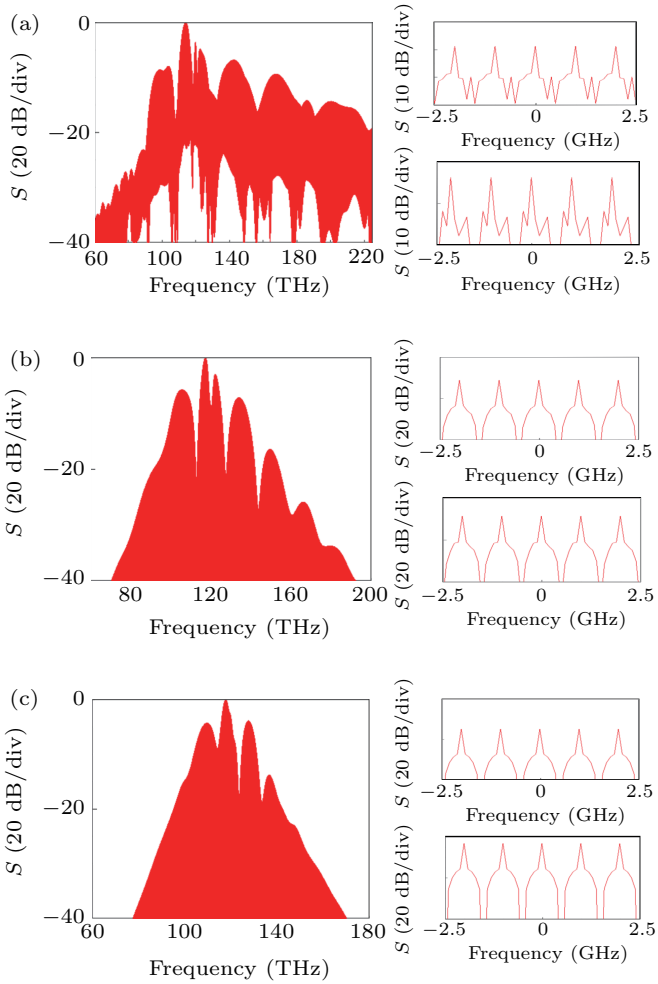


Fig. 9. The OFCs generated by a train of 50 pulses at a repetition rate of 1 GHz for the (a) LP_{01}, (b) LP_{02}, and (c) LP_{12} modes, respectively. The shaded color areas represent the highly dense OFCs. The inserts of panels (a), (b), and (c) show the zoom-in views of the highly dense OFCs at 100 THz (upper) and 120 THz (lower).

4. Conclusion

In summary, we design an MM-TPCF for the MIR SC generation. The influences of the pump pulse parameters on the multimode nonlinear process of the SC generation are investigated. When the pump pulse with $\lambda_0 = 2.5$ μm, $T_0 = 80$ fs, and $P_0 = 18$ kW is coupled into the anomalous dispersion region of the LP_{01}, LP_{02}, and LP_{12} modes of the 3-mm-long MM-TPCF, the highly coherent and octave-spanning MIR SCs can be generated. Finally, based on the generated MIR SCs, the OFCs are obtained when a train of 50 pulses at a repetition rate of 1 GHz is used as the pump source. Our research results can find important applications in optical communication, spectroscopy, metrology, *etc.*

References

[1] Yuan J H, Kang Z, Li F, Zhang X, Sang X, Wu Q, Yan B, Wang K, Zhou X, Zhong K, Zhou G, Yu C, Lu C, Tam Y and Wai P K A 2017 *J. Lightwave Technol.* **35** 2994
[2] Thorpe M J, Hudson D D, Moll K D, Lasri J and Ye J 2007 *Opt. Lett.* **32** 307
[3] Hartl I, Li X, Chudoba C, Ghanta R K, Ko T H, Fujimoto J G, Ranka J K and Windeler R S 2001 *Opt. Lett.* **26** 608
[4] Torres-Company V, Schröder J, Fülöp A, Mazur M, Lundberg L, Helgason Ó B, Karlsson M and Andrekson P A 2019 *J. Lightwave Technol.* **37** 1663
[5] Dudley J M, Genty G and Coen S 2006 *Rev. Mod. Phys.* **78** 1135
[6] North T and Rochette M 2012 *Opt. Lett.* **37** 2799
[7] Dudley J M, Genty G, Dias F, Kibler B and Akhmediev N 2009 *Opt. Express* **17** 21497
[8] Liao M, Yan X, Gao W, Duan Z, Qin G, Suzuki T and Ohishi Y 2011 *Opt. Express* **19** 15389
[9] Price J H V, Belardi W, Monro T M, Malinowski A, Piper A and Richardson D J 2002 *Opt. Express* **10** 382
[10] Agrawal G 2013 *Nonlinear Fiber Optics*, 5th edn. (San Francisco: Academic Press) p. 388
[11] Dudley J M and Taylor J R 2009 *Nat. Photonics* **3** 85
[12] Kaminski C F, Watt R S, Elder A D, Frank J H and Hult J 2008 *Appl. Phys. B* **92** 367
[13] Dudley J M, Provino L, Grossard N, Maillotte H, Windeler R S, Eggleton B J and Coen S 2002 *J. Opt. Soc. Am. B* **19** 765
[14] Herrmann J, Griebner U, Zhavoronkov N, Husakou A, Nickel D, Knight J C, Wadsworth W J, Russell P St J and Korn G 2002 *Phys. Rev. Lett.* **88** 173901
[15] Nicholson J W, Yan M F, Wisk P, Fleming J, DiMarcello F, Monberg E, Yablon A, Jorgensen C and Veng T 2003 *Opt. Lett.* **28** 643
[16] Ranka J K, Windeler R S and Stentz A J 2000 *Opt. Lett.* **25** 25
[17] Town G E, Funaba T, Ryan T and Lyytikainen K 2003 *Appl. Phys. B* **77** 235
[18] Ghosh D, Roy S, Pal M, Pal A, Bhadra S K, McCarthy J, Bookey H and Kar A 2009 *Appl. Opt.* **48** G12
[19] Kubat I, Agger C S, Moselund P M and Bang O 2013 *J. Opt. Soc. Am. B* **30** 2743
[20] Thapa R, Rhonehouse D, Nguyen D, Wiersma K, Smith C, Zong J and Chavez-Pirson A 2013 *Proc. SPIE* 8898
[21] Shi H, Feng X, Tan F, and Wang P 2016 *Opt. Mater. Express* **6** 3967
[22] Domachuk P, Wolchover N A, Cronin-Golomb M, Wang A, George A K, Cordeiro C M B, Knight J C and Omenetto F G 2008 *Opt. Express* **16** 7161
[23] Ou H, Dai S, Zhang P, Liu Z, Wang X, Chen F, Xu H, Luo B, Huang Y and Wang R 2016 *Opt. Lett.* **41** 3201
[24] Zhao Z, Wu B, Wang X, Pan Z, Liu Z, Zhang P, Shen X, Nie Q, Dai S and Wang R 2017 *Laser Photon. Rev.* **11** 1700005
[25] Li Q, Liu L, Jia Z, Qin S, Ohishi Y and Qin W P 2017 *J. Lightwave Technol.* **35** 4740
[26] Xu F, Mei C, Yuan J, Li F, Kang Z, Yan B, Wang K, Sang X, Zhou X, Zhong K and Yu C 2018 *Opt. Soc. of Am.* **W3A** 30

[27] Nguyen H P T, Tong T H and Luo X 2019 *CLEO: Science and Innovations*, March 5–10, San Jose, USA, p. 109
[28] Klimczak M, Michalik D and Stpniewski G J 2019 *J. Opt. Soc. Am. B* **36** A112
[29] Richardson D J, Fini J M and Nelson L E 2013 *Nat. Photon.* **7** 354
[30] Poletti F and Horak P 2009 *Opt. Express* **17** 6134
[31] Salem A B, Trichili A and Cherif R 2016 *Appl. Opt.* **55** 4317
[32] Cherif R, Zghal M, Tartara L and Degiorgio V 2008 *Opt. Express* **16** 2147
[33] Chen Y, Chen Z, Wadsworth W J and Birks T A 2013 *Opt. Express* **21** 17786
[34] Jiang X, Joly N Y, Finger M A, Babic F, Pang M, Sopalla R, Frosz M H, Poulain S, Poulain M, Cardin V, Travers J C and Russell P St J 2016 *Opt. Lett.* **41** 4245
[35] Kubat I and Bang O 2016 *Opt. Express* **24** 2513
[36] Khalifa A B, Salem A B and Cherif R 2018 *Frontiers in Optics*, September 16–20, 2018, Washington DC, USA, p. 18
[37] Eslami Z, Ryczkowski P and Salmela L 2020 *CLEO: Science and Innovations*, March 10–15, 2020, Washington DC, USA, p. 3103
[38] Liao M, Duan Z, Gao W, Yan X, Suzuki T and Ohishi Y 2011 *Appl. Phys. B* **105** 681
[39] Cheng T, Sakai Y, Suzuki T and Ohishi Y 2015 *Opt. Lett.* **40** 2088
[40] Li F, Li Q, Yuan J and Wai P A 2014 *Opt. Express* **22** 27339
[41] Cheng Y, Yuan J, Mei C, Li F, Kang Z, Yan B, Zhou X, Wu Q, Wang K, Sang X, Zhong K, Yu C and Farrell G 2020 *Opt. Commun.* **454** 124380
[42] Hult J 2007 *J. Lightwave Technol.* **25** 820